RESEARCH ARTICLE

Key Points:
- Time series ground deformation over Salt Lake Valley (Utah) has been obtained from satellite InSAR data
- Long-term and seasonal deformation observations, and hydrological records help characterize hydrogeological properties
- Deformation maps and decay coefficients suggest that surface faults disturb groundwater flow and partition hydrological units

Characterization of Hydrogeological Properties in Salt Lake Valley, Utah, using InSAR

Xie Hu[1] (iD), Zhong Lu[1] (iD), and Teng Wang[2] (iD)

[1]Huffington Department of Earth Sciences, Southern Methodist University, Dallas, TX, USA, [2]Earth Observatory of Singapore, Nanyang Technological University, Singapore

Abstract Charactering subsurface aquifer systems is important not only to managing their long-term viability as a stable water source but also to protecting the residences and infrastructures. In particular, understanding how aquifer skeletons deform in response to hydraulic head changes requires hydrogeological parameters such as decay coefficient, storage coefficient, and bulk compressibility. Quantifying these key aquifer properties often requires the analysis of limited water gauge and drilling data. Here we investigate the spatiotemporal correlation between the vertical ground deformation derived by ENVISAT Advanced Synthetic Aperture Radar (ASAR) and Sentinel-1A data sets and available hydrological records in order to improve the aquifer characterization under Salt Lake Valley, Utah. Interferometric synthetic aperture radar results show a clear long-term and seasonal correlation between surface uplift/subsidence and groundwater recharge/discharge, with evidence for the net uplift of 15 mm/year of an area southwest of Salt Lake City for six years. The long-term uplift, bounded by faults and contained within the water discharge area, reflects a net increase in pore pressure associated with prolonged water recharge probably decades ago. The distribution of both previously mapped faults and newly mapped faults within the fields of deformation and the decay coefficient suggests that the faults disrupt the groundwater flow and partition the hydrological units. We also characterize human- and hydrological-triggered deformation by the features of seasonality and the deviation from the exponentially decaying model. By improving our ability to characterize aquifer structures, interferometric synthetic aperture radar analysis of surface deformation in combination with traditional hydrological monitoring data presents an opportunity to recognize and mitigate potential hazards.

1. Introduction

Aquifer systems play an important role as a stable water source, by storing rainfall and snowmelt underground during the recharge process and supplying rivers and/or lakes with water during the discharge process. This is certainly true in the Salt Lake Valley of Utah, where humans rely on groundwater for domestic and municipal uses (Wallace & Lowe, 2009). While extreme changes in climate (e.g., decadal drought or sustained intense precipitation) can disrupt the normal seasonal groundwater balance held in aquifer systems, agricultural and industrial development, and other human activities (e.g., over-pumping and/or injection) are the primary threat to their stability. Changes in aquifer reservoir volumes may manifest as surface deformation, which can be observed using interferometric synthetic aperture radar (InSAR) techniques.

Water recharge and discharge modulate subsurface pore pressure and the effective stress that is usually accompanied by deforming an aquifer skeleton. For example, groundwater removal through pumping has been widely performed for domestic, municipal, industrial, and irrigational uses, which may lead to land subsidence at rates of tens of cm per year associated with the drastic decline of water level (Bell et al., 2002). In addition to removing groundwater from aquifer systems, artificial recharge, or pumping into an aquifer, is sometimes implemented as a technique to manage the long-term removal of water and/or to store water in anticipation of upcoming demand, which may exert regional uplift (Amelung et al., 1999; Chaussard et al., 2014; Lu & Danskin, 2001; Schmidt & Bürgmann, 2003). The resulting deformation can generally be classified as either (1) elastic (recoverable) strain that is typically associated with cyclic compression and dilation of the aquifer skeleton or (2) inelastic strain that is often associated with irreversible subsidence following long-term discharge when the effective stress is larger than the preconsolidation stress (e.g., Amelung et al., 1999; Casagrande, 1932, 1936; Galloway et al., 1999; Miller et al., 2017; Miller & Shirzaei, 2015).
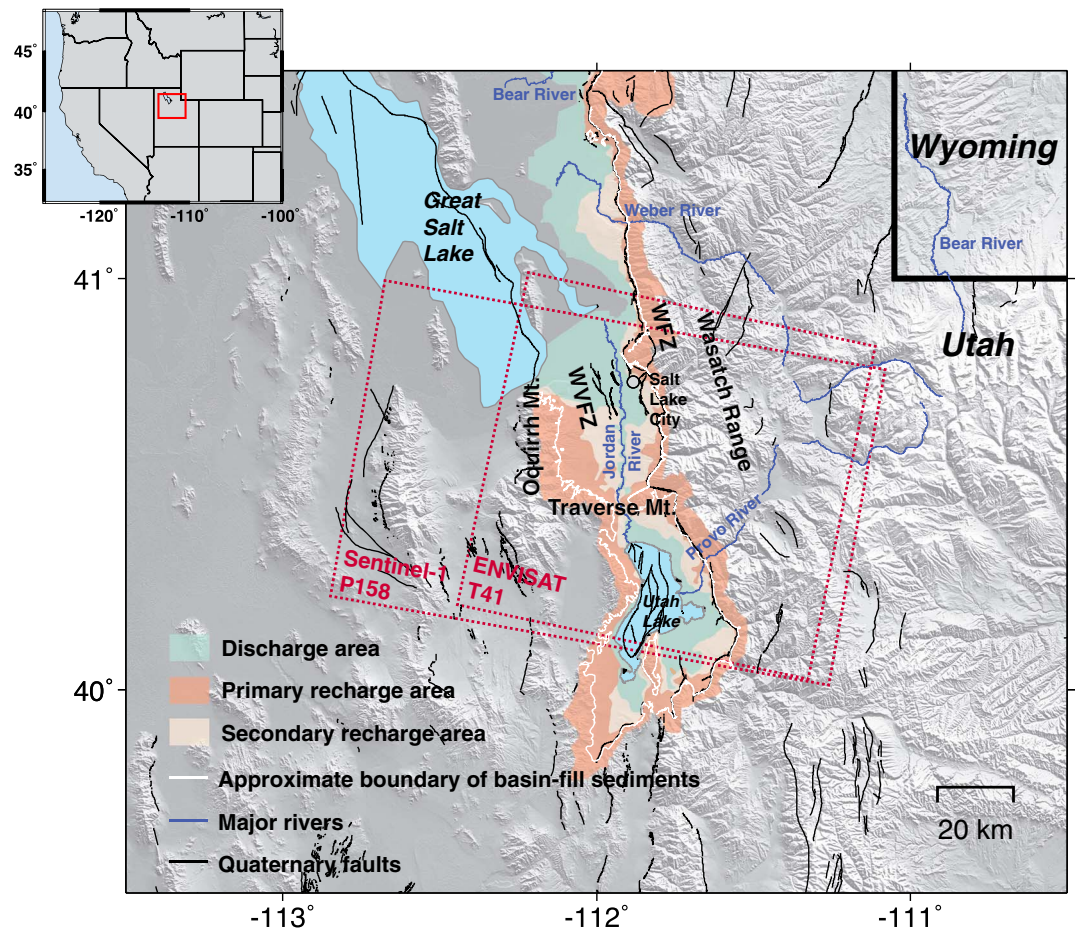
Figure 1. Locations of groundwater discharge, primary recharge and secondary recharge areas in Salt Lake Valley, Utah. The white lines delineate the boundary of basin-fill sediments, the blue lines show the major river channels, and the black lines show the known faults. The coverage of descending SAR tracks ENVISAT Track 41 (T41) and Sentinel-1A Path 158 (P158; cropped) are marked with red dotted rectangles.

Spaceborne multitemporal InSAR observations represent a useful method to quantify ground deformation due to water level changes with mm/year accuracy. For example, vertical deformation and associated hydrological properties have been studied for cities built in the desert, such as Las Vegas (Amelung et al., 1999), Tucson (Kim et al., 2015; Miller et al., 2017), and Phoenix (Miller & Shirzaei, 2015); for valleys with rapid urban and industrial development, such as Santa Clara Valley, California (Schmidt & Bürgmann, 2003); and in valleys with heavy agricultural production, such as San Luis Valley, Colorado (Chen et al., 2016; Reeves et al., 2014). In this study, we combine InSAR data with water level data to derive hydrogeological properties in Salt Lake Valley, Utah. Based on the spatiotemporal correlation between vertical ground deformation and the water discharge and recharge processes, we discuss both natural and anthropogenic triggers to the observed deformation in the valley.

2. Hydrogeologic Settings and Properties in Salt Lake Valley

Salt Lake Valley, Utah, which includes the state capital Salt Lake City, is the commercial, industrial, and financial center of the State of Utah. One third of the state's population (~3 million) is concentrated in the valley. The basin is bounded on the west and east by the generally parallel, north-south trending mountain ranges, Oquirrh Mountains and Wasatch Range, respectively (Figure 1). To the south, the west-east trending Traverse Mountains bound the valley. The 70-km-long Jordan River traverses the center of Salt Lake Valley, connecting two remnants of prehistoric Lake Bonneville (30,000–14,000 years before present)—the Great Salt Lake and Utah Lake. The well-known Wasatch fault zone (WFZ) is situated along the mountain front of the Wasatch

Range, and the West Valley fault zone (WVFZ) is located within the valley. The basin-fill deposits (boundary outlined by the white line in Figure 1) consist of the surficial and near-surficial unconsolidated Quaternary deposits by Lake Bonneville, and the underlying generally unconsolidated to semiconsolidated Tertiary deposits (Arnow et al., 1970; Thiros et al., 2010). The main basin-fill deposits are vertically stratified into both shallow aquifers and deeper aquifers, with the latter marked by discontinuous layers of fine-grained deposits that inhibit the downward movement of groundwater.

Within the boundary of basin-fill sediments, the aquifer systems can be classified into three distinct areas: primary recharge area, secondary recharge area, and the discharge area (Figure 1). The primary recharge area is in the uplands along the mountain fronts where there is an absence of confining fine-grained deposits and a downward hydrologic gradient flow (Figure S1). The secondary recharge area, usually at a lower elevation from the primary recharge area, such as a mountain bench, contains both unconfined and confining layers in the subsurface. The hydraulic gradient is again downward and groundwater flows into deeper layers and/or toward the discharge area. Annual groundwater recharge to the aquifer systems is about 0.4 km^3 (Lambert, 1995; Thiros et al., 2010). Major sources of recharge include subsurface inflow from mountain streams (45%) and precipitation infiltration (21%; Thiros et al., 2010). In the discharge area, the hydraulic gradient is reversed, enabling groundwater to flow up into a confined area or to exit to the surface (Figure S1). Naturally occurring discharge to the surface occurs under several circumstances: where the water table intersects the surface, discharge around the unconfined aquifer occurs into streams, canals, and the Jordan River; where the surface elevation is low in the vicinity of the Great Salt Lake, discharge around the confined aquifer occurs at the northern part of the valley; finally, some water is lost through evapotranspiration. When there is sufficient natural pressure, water reaches the surface at artesian wells. Anthropogenic withdrawal of water from the systems may also be referred to as groundwater discharge, but a water well could be located in any of the three areas (primary recharge, secondary recharge, or discharge area) under the right conditions. The main components of groundwater discharge include seepage into streams (43%) and well withdrawal (33%; Thiros et al., 2010).

The confined aquifer consists primarily of Quaternary deposits (0 to over 600 m) of clay, silt, sand, and gravel. Above the confined aquifer is a confining layer composed of individual Quaternary deposits of fine-grained clay and/or silt that creates an impermeable layer (Figure S1). The confining layer is between 12 and 30 m thick with its top 15 to 46 m below the land surface. There might be a shallow unconfined aquifer overlying the confining layer, and it is sometimes hard to differentiate between them. The shallow unconfined aquifer is primarily composed of fine-grained sediments, and it has a maximum thickness of 15 m (Snyder & Lowe, 1998; Wallace & Lowe, 2009). This study focuses on the vertical ground deformation and the related hydrodynamics of the confined and semiconfined aquifers, mainly over the water discharge area and secondary recharge area.

The groundwater system in Salt Lake Valley's basin-fill deposits includes a shallow aquifer that is separated from a deeper aquifer by discontinuous layers or lenses of fine-grained materials. The existence and different thickness of the embedded clay lenses with low hydraulic conductivity may result in various time scales of delay for the equilibration to hydraulic head changes. The delayed response can be characterized by modeling the long-term vertical deformation as an exponential function of time (Chaussard et al., 2014; Miller et al., 2017; Miller & Shirzaei, 2015):

$$d_{long-term}(t) = M(e^{kt} - 1) \tag{1}$$

where $d_{long-term}(t)$ is long-term vertical deformation at time t, M is the magnitude coefficient ($M > 0$ when net subsidence and $M < 0$ when net uplift), and k is the decay coefficient (between -1 and 0), which is related to the compressibility and hydraulic conductivity of the aquifer-system skeleton and is used to simulate the decelerated deforming process. A smaller decay coefficient k (closer to -1) leads to a faster equilibration (leveling off), suggesting a faster response to a given hydraulic head change in a long-term view.

Storage properties are also important hydrological parameters for water management. The specific storage coefficient S_s for a confined aquifer is the amount of water drained from the compressed aquifer systems with per unit decline in hydraulic head, per unit volume of the aquifer (Riley, 1969; Saar & Manga, 2003):

$$S_s = \rho g(\alpha + n\beta) \tag{2}$$

where ρ is the water density, g is the gravitational acceleration, α is the bulk aquifer compressibility (at constant vertical stress and zero lateral strain), n is the porosity, and β is the compressibility of water (4.6×10^{-10} m^2/N). The bulk aquifer compressibility α describes the relative volume change of the aquifer skeleton in response to a pressure change.

The dimensionless storage coefficient for a confined aquifer characterizes the volume of water drained per unit decline in hydraulic head, per unit area of the aquifer. The storage coefficient S is the vertical integration of the specific skeletal storage coefficient (Riley, 1969), assuming that the water compressibility is negligible with respect to the deformation of the aquifer systems,

$$S = S_s b \tag{3}$$

where S_s is the skeletal specific storage coefficient and b is the aquifer thickness (Chaussard et al., 2014; Riley, 1969).

The storage coefficient can be classified into inelastic or elastic when the effective stress is larger or smaller than the preconsolidation stress, which is subject to the historical hydraulic head levels and ground deformation. The hydraulic head can be obtained from the water level measurement at piezometric wells when the piezometer bottom is fixed. We focus on characterizing the elastic storage coefficient because no long-term large compaction associated with sustained water level declines has been observed in our study area (discussed in section 5.2). The elastic storage coefficient can be solved by the linear regression:

$$S = \Delta d_e / \Delta h \tag{4}$$

where Δd_e is the elastic (seasonal) vertical deformation and Δh is the head change (Chaussard et al., 2014; Chen et al., 2016; Miller et al., 2017; Miller & Shirzaei, 2015; Riley, 1969).

Different from the decay coefficient, the estimation of storage coefficient (S), specific storage coefficient (S_s), and bulk aquifer compressibility (α) require water level data in addition to the vertical deformation measurements. And more importantly, water level data with both a high sampling rate and a distinct peak-to-trough amplitude are highly desired for enhancing the signal-to-noise ratio.

3. Methods

3.1. Multitemporal InSAR Analysis

Forty ENVISAT Advanced Synthetic Aperture Radar (ASAR) strip mode data (2004–2010) and 20 Sentinel-1A interferometric wide swath mode data (2015–2016) were used to derive the deformation field over the study area based on multitemporal InSAR analysis (e.g., Berardino et al., 2002, Ferretti et al., 2001, Hooper, 2008, Hu et al., 2016, Shirzaei et al., 2017). ENVISAT's heading and incidence angles were −167.83° and 22.78°, and Sentinel-1A's heading and incidence angles were −166.38° and 41.97°. We processed the ENVISAT data using GAMMA software. We processed the Sentinel-1A data burst by burst and then merged them into one interferogram. The phase discontinuity was corrected from burst-overlap interferometry (Jiang et al., 2017). A set of 126 ENVISAT interferograms with perpendicular baselines less than 300 m and temporal intervals fewer than 500 days and 82 Sentinel-1A interferograms with perpendicular baselines less than 250 m and temporal intervals fewer than 180 days were chosen for time series analysis (Figure S2). The topographic phase component of each interferogram was simulated by 2000 SRTM digital elevation model (DEM).

The urbanized basin terrain from Salt Lake City to Bluffdale maintains good InSAR coherence. However, it is mostly isolated by the mountainous areas to the west, east, and south sides, as well as the wetland area in the vicinity to the Great Salt Lake to the east side, where the radar phase values are poorly correlated in time or incoherent in space (Figure S3). It results in very narrow channels (bounded by mountains) with decent coherence to connect the basin terrain to other urban areas to the north (e.g., North Salt Lake) and the south (e.g., Lehi). This spatial configuration of surface features may lead to phase jumps at the north and south mouths when using a general phase unwrapping routine. To address this issue, pixels with an amplitude dispersion (the ratio between the standard deviation and the mean of the SAR amplitude) of less than 0.35 and an averaged coherence larger than 0.5 were chosen as coherent targets (CTs) for ENVISAT data. The corresponding thresholds were 0.15 and 0.7 for Sentinel-1A data. The window used to estimate the spatial coherence is 15 by 5 and 6 by 23 pixels for ENVISAT and Sentinel-1A data, respectively. Unwrapping was then

performed exclusively on those CTs (Ferretti et al., 2001; Hooper, 2010; Hu et al., 2016). Finally, the deformation signals were resolved by culling out the DEM errors, atmospheric phase screen, and orbital artifacts inherent in each interferogram based on their spatial and temporal signatures (Hu et al., 2016).

The inconsistency of DEM sources and/or DEM errors can introduce phase artifacts, which may be expressed as spurious deformation signals (e.g., Hu et al., 2016). This is particularly the case for the ENVISAT data set due to its varied baseline configurations. Therefore, ENVISAT interferograms (red connecting lines in Figure S2a) with relatively larger perpendicular baselines (>100 m) and smaller time spans (<180 days) were selected to isolate the DEM errors (e.g., Lu & Dzurisin, 2014, Massonnet & Feigl, 1998), assuming that the phase is dominated by the error in DEM rather than ground deformation. Interestingly, the map of DEM errors highlights a nearly 1-km^2 area (40°45′52″N, 111°53′20″W) with an error of more than 15 m over downtown Salt Lake City; this observation is consistent with the anomaly in the differential DEM map between 2000 SRTM DEM and 2006 LiDAR DEM (Figure S4). Historic aerial photographs show no visible change for the high-rise buildings clustered in downtown Salt Lake City. The agreement between these two independent estimations suggests that C-band SRTM radar data may contain height errors probably due to geometric artifacts and/or unwrapping errors associated with the urban landscape.

We assume that the derived deformation in the basin is mainly vertical, because the basin accommodates classic normal faults with steep dip angles ~60–86°W (Black et al., 1996). In addition, the burst-overlapping interferometry of Sentinel-1A data (~2 cm accuracy; Jiang et al., 2017), which is sensitive to deformation along the azimuth direction, also suggests no detectable horizontal deformation in the approximate north-south direction (Figure S5). All deformation mentioned below, without specification, has already been projected into the vertical direction from the radar line-of-sight direction.

3.2. Separation of Long-Term and Seasonal Deformation Signatures

The long-term deformation velocity of an aquifer is often related to prolonged hydraulic head changes, in contrast to the seasonal deformation considered a short-term response to groundwater redistribution. To characterize the time series deformation, we need to separate out the long-term deformation from seasonal fluctuations. We first fit the nonlinear component of time series deformation at each CT using harmonic series to roughly simulate the periodicity of deformation behavior. The merits of this method are that we can obtain the seasonal deformation signal agreed with given apparent frequency. On the basis of our observations that the processes of water discharge (Figure S6) and recharge (Figure S7) take a period of one year, and that water levels are also annual (Figure S8), we consider the pixel with deformation seasonality feature of deformation when the derived deformation waveform contains 10 to 14 peaks or troughs during the six-year period from 2004 to 2010; otherwise, the pixel is flagged without seasonality. The more sinusoidal functions used, the better fit with the observation. However, here our purpose is to extract the apparent seasonality. If we use many independent sinusoidal functions, the fit results will capture the high-frequency wiggles in the time series and introduce unexpected peaks or troughs. In our study area, we determined that using three independent sinusoidal functions best simulated the apparent seasonality. For pixels with the seasonality feature of deformation, the remainder after subtracting the harmonic series from the original time series is considered to be the long-term signature. Using a sinusoidal function of time to perform the InSAR time series analysis is not new (e.g., Agram et al., 2013, Agram & Simons, 2015, Fattahi et al., 2017, Ferretti et al., 2000, Reinisch et al., 2016, Riel et al., 2014). However, our method has two advantages: first, not all targets deform with seasonality so we justify if the time series deformation contains the seasonality or not rather than force the deformation pattern of all targets exclusively using sinusoidal wave, and second, we allow year-by-year variations in amplitude and frequency using the superposition of three independent sinusoidal functions but constrain the waveform within the desired apparent frequency.

3.3. Estimation of Aquifer Properties From Surface Deformation and Groundwater Levels

The decay coefficient, k, which is used to describe the decelerated deforming process, was estimated from six years of deformation measurements of ENVISAT data (2004–2010) using a least squares inversion technique. Although the Sentinel-1A data set provides deformation measurements between 2015 and 2016, the limited observation interval was too short to constrain the decay coefficient. After removing the seasonal component (if any), the remaining long-term deformation component was used to derive the decay coefficient at each CT based on equation (1).
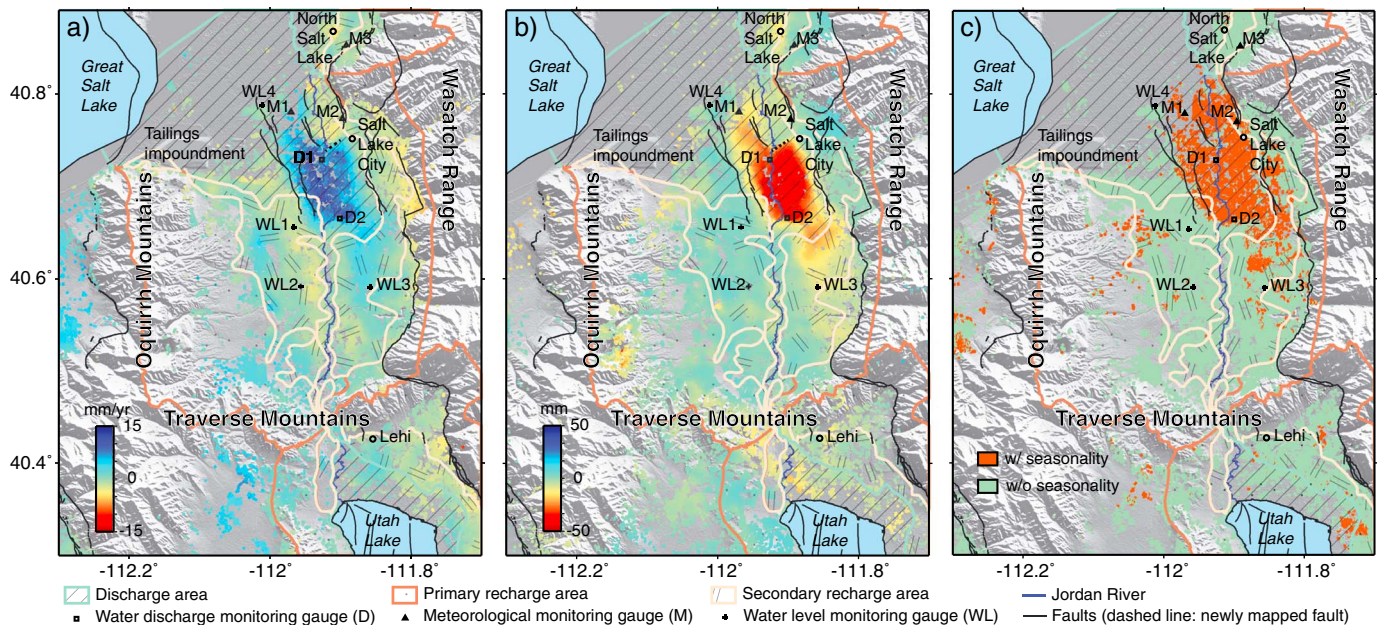
Figure 2. Vertical deformation and its feature of seasonality over Salt Lake Valley. (a) Long-term deformation velocity derived from ENVISAT data set between September 2004 and October 2010 indicating uplift in blue. (b) Seasonal deformation derived from Sentinel-1A data set between April and August 2015 indicating subsidence in red. (c) Map of deformation seasonality. The squares, triangles, and crosses represent the locations of the water discharge monitoring gauges (D1 and D2), meteorological monitoring gauges (M1 to M3), and water level monitoring gauges (WL1 to WL4), respectively. The black lines show the known faults. The black dashed line (west of Salt Lake City) delineates the deformation discontinuity, which may correspond to a blind fault segment. Water discharge, primary recharge, and secondary recharge areas are shown with the specified patterns.

Deformation and water level measurements provide a straightforward method to solve for the storage coefficient: first, pick up the peaks and troughs in each water level time series and resample the deformation for the common dates; second, calculate the change between adjacent estimates to obtain seasonal variations; and third, fit the linear regression that pass through (0, 0), and then the slope corresponds to storage coefficient (Chaussard et al., 2014). However, this method is only useful when the time series ground deformation is in phase with water levels at a similar frequency; that is, there is no phase delay for the surface movement in response to head changes. An alternative method is to find the optimal storage coefficient S and time lag τ that minimize the objective function $\|d_{\text{detrend}}(t + \tau) - S \times h_{\text{detrend}}(t)\|$ (Chen et al., 2016), where $d_{\text{detrend}}(t)$ and $h_{\text{detrend}}(t)$ are the detrended ground deformation and water levels at time t, respectively. Time lags may occur and differ for the hydrologic units to equilibrate to the additional stress. The length of time lag depends on factors such as the specific storage, the thickness, and the vertical hydraulic conductivity of each stratum (Chen et al., 2016; Riley, 1969).

4. Results

4.1. Spatial Features of the Deformation Field

The velocity map derived from ENVISAT data indicates six-year (2004–2010) net uplift southwest of downtown Salt Lake City at an average rate of 15 mm/year (Figure 2a). The uplifting area of interest (UAOI) is constrained within the confined discharge areas, which to some extent confirms the validity of predefined aquifer boundaries. Nevertheless, subsidence occurs from April to August 2016 according to Sentinel-1A results (Figure 2b) at the same location of the net uplift. The summer months' deformation represents the seasonal amplitude. The similar spatial distribution of the deforming signatures derived from these two independent data sets suggests that the observed long-term uplift and seasonal oscillation originate from the same aquifer unit.

The boundaries of the UAOI are also coincident with the locations of a few known faults, suggesting that these faults define and perhaps control the groundwater flow. We also identify a sharp discontinuity (black dashed line in Figures 2a and 2b) at the northern tip of the UAOI, and we suspect that this indicates a

blind fault orthogonal to the preexisting ~30° northwest trending fault west of downtown Salt Lake City, probably a step-over that bridges the parallel WFZ at the base of Wasatch Range and WVFZ to the west side of Jordan River.

CTs exhibiting seasonal deformation (red points in Figure 2c) are concentrated around downtown Salt Lake City, bounded by inner-valley WVFZ and mountain-front WFZ, and the seasonal cluster contains our UAOI. Additionally, we have identified two localized subsiding sites shown without seasonality in North Salt Lake and Lehi (locations marked with black circles in Figure 2, see details in section 5.1 and Figure 6).

4.2. Time Series Vertical Deformation Versus Water Discharge and Precipitation

The long-term trend from 2004 to 2010 indicates clear net uplift. Time series InSAR analysis allows us to further discern the seasonal dynamics of the aquifer basin. The high frequency of Sentinel-1A data sampling improves our understanding of surface movement to less than one-month scale (when we only consider highly coherent acquisitions) over this valley.

To assess the correlation between groundwater and seasonal ground deformation, we collected water discharge time series data at two gauges, D1 and D2 (squares in Figure 2), and precipitation time series data at three gauges, M1 to M3 (triangles in Figure 2), and compared the gauge data to the InSAR-derived deformation of CTs coinciding with the gauge locations. Groundwater discharge into streams accounts for almost half of the total amount of discharge in Salt Lake Valley (Thiros et al., 2010) and can be approximated by hydrographs of streams at low elevations receiving the water discharge, such as the Jordan River. The two streamflow monitoring gauges (D1 and D2) are located around the boundary of the UAOI along the river. We observed a clear phase shift between ground deformation and the water discharge rate at the two gauges (Figure S6), prompting us to consider the modulation associated with the water recharge process, and specifically precipitation. Three meteorological monitoring gauges (M1, M2, and M3) are located in the discharge area: one (M3) is located in North Salt Lake, and the other two (M1 and M2) are equidistant to the axis of the Jordan River at two sides, with M1 on the west side located at the northern tip of the UAOI. Precipitation follows seasonal variation and peaks in winter (Figure S7).

To better understand the dynamics of hydrologically driven deformation without the direct water level measurements of the confined aquifer well, we need to consider both water discharge and recharge processes. The gauge data are surface water measurements. As it takes time for surface water to discharge from and recharge to the confined aquifer, the phase shifts between water levels and water discharge/precipitation are reasonably present. Extraction of the deformation measurements of the CTs near the water discharge monitoring gauge D1 reveals a net uplift averaging 15 mm/year from 2004 to 2010 (Figure 3a). We also observed a seasonal ground oscillation with subsidence during the midspring and summer months (March/April to August) and uplift during fall and winter months, with the largest peak-to-trough magnitude of more than 40 mm (Figure 3b). We consistently observed such seasonal signature during both time intervals. Assuming that the meteorological monitoring gauge at M1 depicts the precipitation received by the gauge 6.8 km southward at D1, we compared the seasonal deformation component with water discharge rate and precipitation. The ground uplift and subsidence seem related to hydrological processes (such as precipitation and water discharge); all exhibit seasonal signatures. The influx of water, such as the infiltration of precipitation into the subsurface, can elevate the pore pressure, thereby reducing the vertical effective stress on the skeletal matrix of the aquifer and exerting regional uplift (e.g., Schmidt & Bürgmann, 2003); when the amount of precipitation declines, the water discharge (such as seepage to the lower elevation Jordan River and Great Salt Lake and anthropological groundwater extraction) exceeds influx, resulting in an elastic response to the reduction of pore pressure and an increase of the vertical effective stress, expressed as regional subsidence through the settling of grains.

4.3. Long-Term Decay Coefficient

The decay coefficient describes the long-term delayed ground response to hydraulic head changes based on the exponential fitting of equation (1). The characteristic time scale of the exponential decay can be taken from the absolute value of the inverse of decay coefficient. To enhance the robustness, we only considered those pixels with a root-mean-square error (RMSE) of the best fitting exponential regression of less than 0.8 cm. The distributions of fault systems on the maps of decay coefficient (Figures 4a and 4b) and
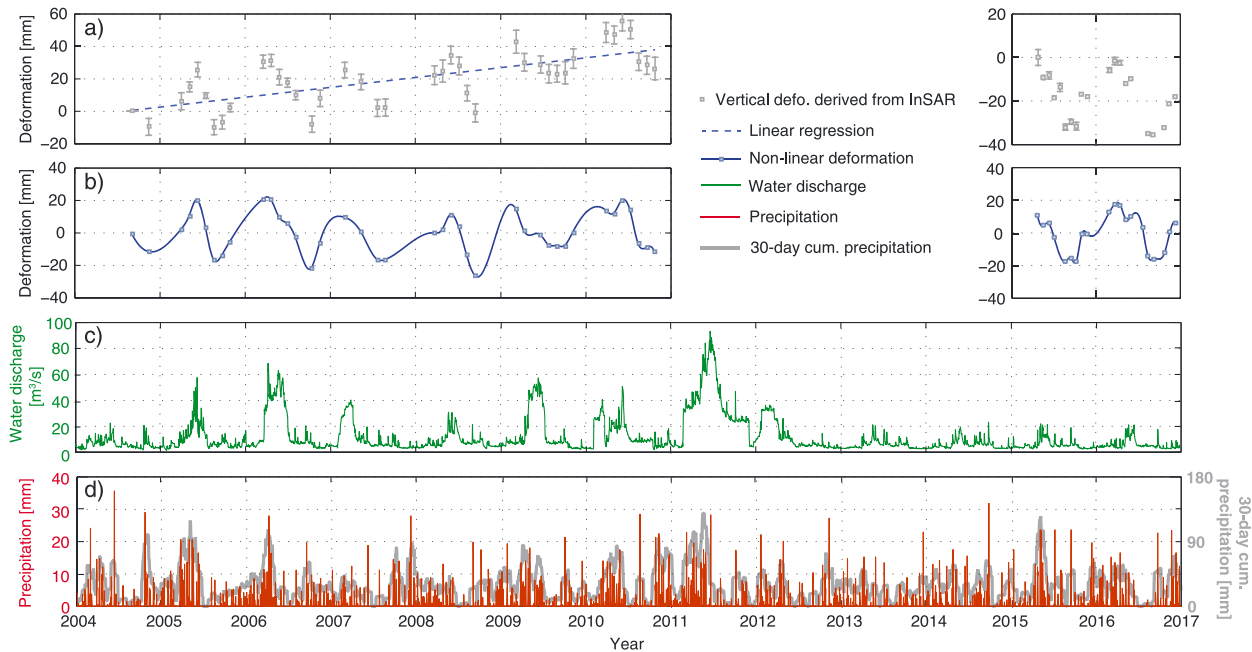
Figure 3. Time series ground deformation (at location D1), water discharge (D1), and precipitation (M1). (a) InSAR-derived deformation (gray squares) and its linear fitting (dashed blue line). The error bars are the standard deviations of the deformation estimates within 700 m of gauge D1. (b) Linearly detrended/seasonal deformation (blue squares) and the spline fitting (solid blue line). In (a) and (b), the left panels are the results of ENVISAT (available for 2004–2010) and the right panels are the results of Sentinel-1A (available for 2015–2016). (c) Water discharge (green line). (d) Daily precipitation (red line, referring to the left y axis) and 30-day cumulative precipitation (gray line, referring to the right y axis).

deformation velocity (Figures 2a and 2b) suggest that the faults partition the hydrological units and control the deformation field. In particular, besides the ~60° northeast trending fault unveiled by the deformation velocity map, we have also identified another previously unknown ~30° northwest trending fault from the decay coefficient map, all of which together provide a complete view of the fault configurations in the area of Salt Lake City.

Within the area exhibiting seasonal deformation (red dotted area in Figure 2c; yellow dotted line area in Figure 4a), the northern and southern areas at the mountain front occupy a smaller decay coefficient, suggesting a faster response to a given hydraulic change than the central section (Figure 4a). The negative values of coefficient M suggest net uplift, and the positive values suggest net subsidence (Figure 4b), which is consistent with the map of long-term deformation velocity (Figure 2a). The decay coefficient of the UAOI is mainly in the range between −0.1 and −0.01, suggesting a time constant of 10 to 100 years. This exponential fitting is designed to simulate the decaying process. Large RMSE (Figure 4c) accompanying the exponential fitting generally result from either substantially fluctuated deformation or the accelerated or quasi-linear trend of deformation that we discuss further in section 5.1.

4.4. Storage Coefficient and Bulk Compressibility

Accurate derivation of the aquifer storage coefficient requires water level measurements. However, many long-term water leveling gauges in this region only record measurements once a year, and even worse, generally in the same season (February or March). Only four gauges (locations are indicated as crosses in Figure 2) provide frequent enough measurements to estimate the storage coefficient: WL1, WL2, and WL3, with nearly daily measurements from the U.S. Geological Survey throughout the entire InSAR acquisition timespan, and WL4 with nearly monthly measurements from the Utah Geological Survey during 2009–2010.

The input detrended water level $h_{detrend}(t)$ is simply the nonlinear component. However, the parameterization of input detrended deformation $d_{detrend}(t)$ depends on whether or not it includes a seasonal signal. If seasonality exists, the detrended deformation is considered to be the seasonal component simulated by
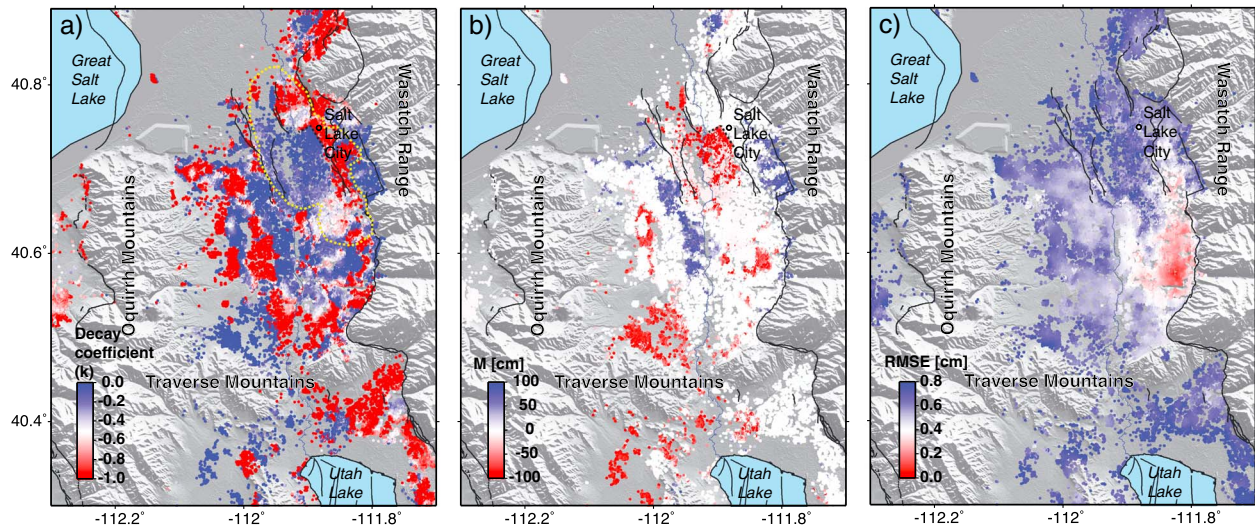
Figure 4. Exponentially decaying deformation explained by $d(t) = M(e^{kt} - 1)$. (a) Decay coefficient k. Blue (closer to 0) means slower equilibration, and red (closer to -1) means faster equilibration to the hydraulic head change. (b) Magnitude coefficient M. Red (negative value) means net uplift, and blue (positive value) means net subsidence. (c) RMSE of the exponentially decaying model. The black solid lines are known faults. The black dashed lines (west and south of Salt Lake City) in (a) and (b) are newly mapped faults in this study. The yellow dotted line area in (a) highlights the seasonally deforming area.

the superposition of three sinusoidal functions; otherwise, the spline interpolation of the linearly detrended deformation was applied. The water level data at WL2 and WL3 exhibit periodic seasonal variations (yellow lines in Figures 5b and 5c), and we identify targets deformed with seasonality in the vicinity of WL2 and WL3 (Figures 5b and 5c). Water level at WL1 does not show evident seasonal variation, and coincidently, no target around this gauge has been identified with seasonal deformation (Figure 5a). Nevertheless, WL4 only has one-year water level data and the existence of seasonality in deformation during this year has not been determined, so we use the spline interpolation of the linearly detrended deformation (Figure 5d). Original time series deformation and water level can be found in Figure S8.

Considering that the period of seasonal deformation and water level is around one year, we set the delay time τ from 0 to 365 days to avoid aliasing. The estimated storage coefficients from well data (Thiros, 2003) range between 0.0005 and 0.1 and are taken as the search window for the storage coefficient (S). The best fit results are shown in Table 1. WL2, in the central south of the valley, occupies the smallest storage coefficient (0.002), while WL4, in the wetlands near Great Salt Lake, has a greater storage coefficient (0.0668), suggesting a larger
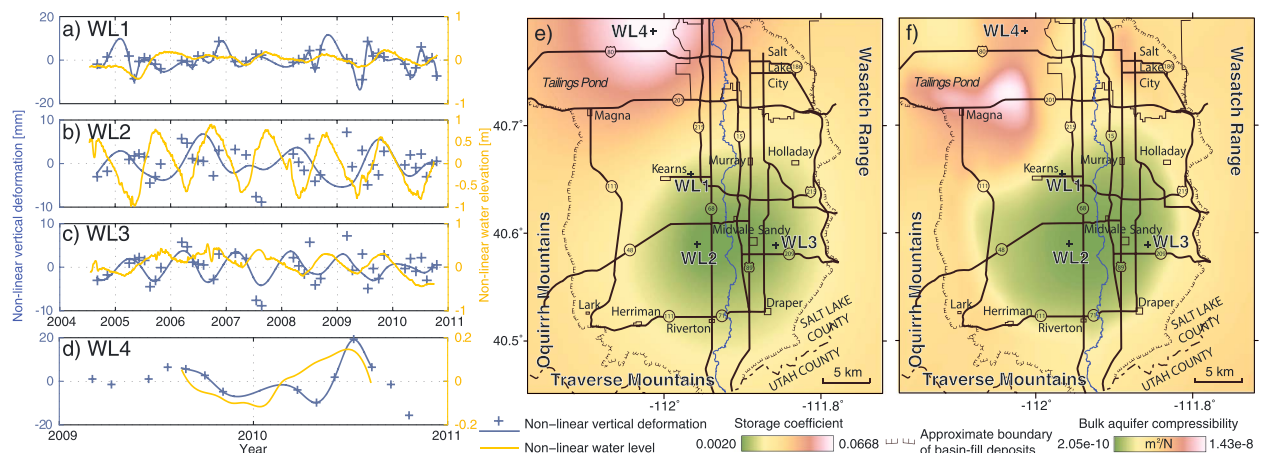

Figure 5. The derived hydrogeological properties. (a–d) Nonlinear vertical deformation in comparison with nonlinear water heads at WL1–WL4. The blue crosses and lines show the detrended deformation in millimeters. The yellow lines show the detrended water level measurements in meters. Original measurements are shown in Figure S8. (e) Storage coefficient interpolated by four estimates at WL1–WL4. (f) Bulk aquifer compressibility considering nonzero water compressibility.

Table 1
Hydrogeological Properties at Water Level Gauges (WL1–WL4)

Site	Lon W (deg)	Lat N (deg)	S	τ (days)	Res. (mm)	b (m)	S_s (m^{-1})	n	α (m^2/N) (negligible β)	α (m^2/N) (nonzero β)
WL1	111.97	40.65	0.0116	306	4.0	631	2e−5	0.1187	2e−9	1.95e−9
WL2	111.96	40.59	0.0022	239	3.0	879	3e−6	0.1392	2e−10	2.36e−10
WL3	111.86	40.59	0.0047	120	1.9	614	8e−6	0.1493	7e−10	7.31e−10
WL4	112.02	40.79	0.0668	43	5.8	706	9e−5	0.0799	9e−9	8.96e−9

Note. S is the storage coefficient, τ is the delay time between the detrended ground deformation and head changes, Res. is the residual of the optimal solution for $\|d_{\text{detrend}}(t + \tau) - S \times h(t)\|$, b is the aquifer thickness that approximated by the thickness of unconsolidated and semiconsolidated sediments, S_s is the specific storage, n is the porosity, and α is bulk aquifer compressibility. The locations of the sites, b, and n are priori-knowns, and the other parameters are derived.

amount of groundwater communication at WL4 in response to given head change. The interpolated map of storage coefficient is shown in Figure 5e.

WL4 occupies the smallest time lag of 43 days, while the time lags for WL1–WL3 range between 120 and 306 days. A lengthy time lag may suggest slow infiltration and slow drainage of the clay lenses around the wells. Aquifer thickness was approximated by the thickness of the unconsolidated and semiconsolidated deposits (digitized from the isopach map; Figure S9a; Arnow & Mattick, 1968; Mattrick, 1970), which includes the Quaternary and partial Tertiary deposits. The thickest (~1,220 m) unconsolidated and semiconsolidated sediments are located in the northwest and northeast parts of the valley. It thins toward the central valley (~600 m) and thickens again gradually toward the south (~800 m). The thinnest (<300 m) part is located along the margins of the valley. We apply basin-wide porosity estimates (Figure S9c) ranging between 0.06 and 0.25 from Starn et al. (2015). In agreement with the compositions of unconsolidated to semiconsolidated clay, silt, sand, gravel, tuff, and lava of the Tertiary- and Quaternary-age basin-fill deposits in Salt Lake Valley (Thiros et al., 2010; Wallace & Lowe, 2009), the derived specific storage coefficient S_s (Figure S9b) and the bulk aquifer compressibility α (Figure 5f) are in a reasonable range for these general sediment types, such as clay, silt, and gravel (Chaussard et al., 2014; Domenico & Mifflin, 1965; Hanson, 1989; Nelson, 1982; Neuman & Witherspoon, 1972; Sneed, 2001; Sneed et al., 2007). The S_s and α of the UAOI southwest of Salt Lake City are 3.8×10^{-5}/m and 1.0×10^{-9} m^2/N, respectively. Given the biases due to the water compressibility, the resulting values for bulk aquifer compressibility α are of the same order, which are mainly influenced by the values for the specific storage S_s because the product of porosity and water compressibility is negligible. The map of aquifer hydrogeological properties can be enhanced if more monthly/seasonally acquired water level data in this region become available.

5. Discussion

5.1. Localized Anthropogenic Deformation and Basin-Wide Hydrogeologic Effects

We observed two localized subsiding sites over the industrial fields in North Salt Lake and the foot of the Traverse Mountains in Lehi. Both sites are located in areas with no seasonal deformation and with large RMSE from the exponentially decaying model. The North Salt Lake site shows continuous quasi-linear subsidence at a rate of ~20 mm/year, which accelerated during 2015–2016 (Figure 6d) compared with the period of 2004–2010 (Figure 6a). One meteorological monitoring gauge (M3 in Figure 2) is located 2 km southeast of this site. However, we do not see a correlation between the nonlinear ground deformation and precipitation (Figure 6b), suggesting that the deformation here is less likely to be influenced by natural hydrological process. The aerial image shows a group of round-top infrastructures over the subsiding site at North Salt Lake (Figure 6c), probably related to industrial production, suggesting that human activities are potentially responsible for the observed subsidence. We also observed an actively (throughout 2015–2016) subsiding site (Figure 6e) near an electronics manufacturing company in Lehi; however, such drastic subsidence has not been identified in the 2004–2010 results. Surface fissures started to develop dramatically between 2010 and 2013 (Figure 6f) and continued growing through July 2016 or afterward. An aging of asphalt may be another reason for the fissures.

The observed localized subsidence shows different deformation patterns compared with the time series over the confined aquifer. The temporal features of seasonality and the residuals of exponentially decaying model may be used to characterize the deformation related to both hydrological processes and industrial
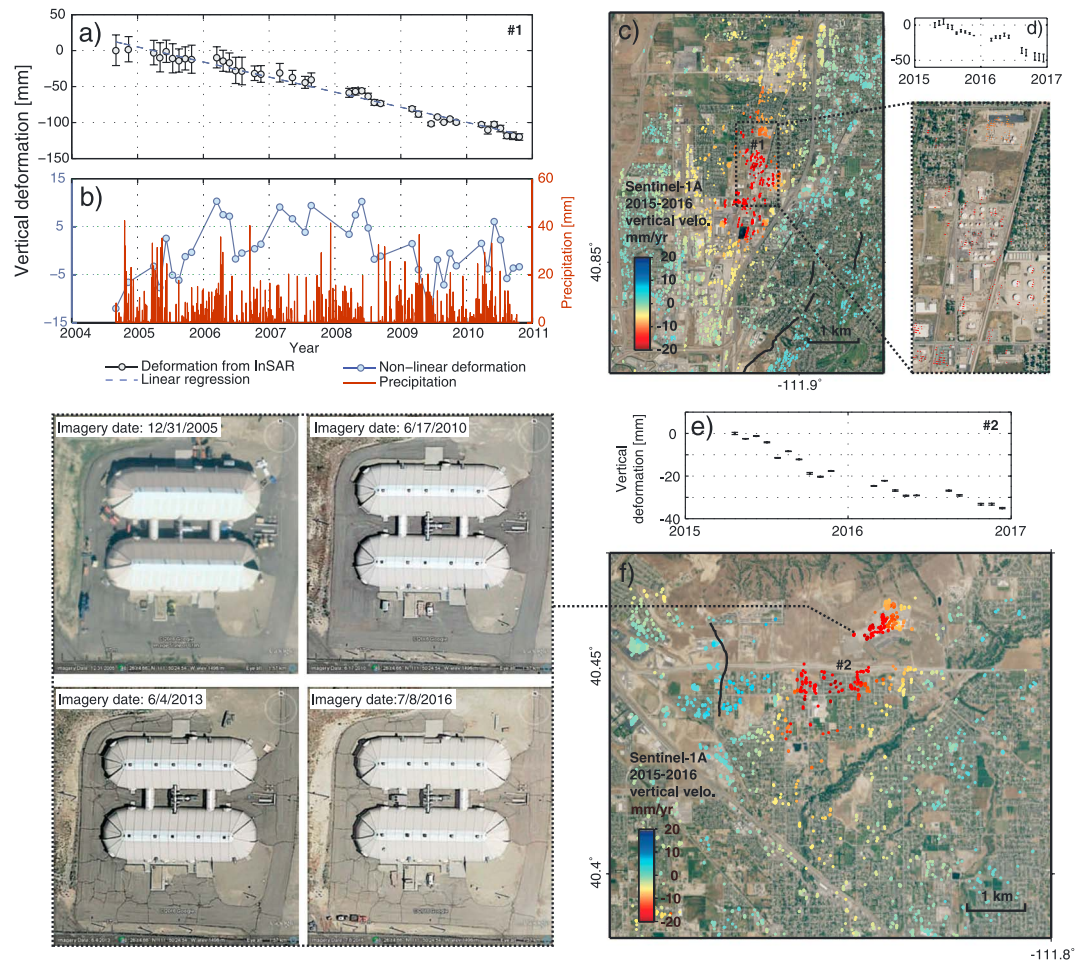
Figure 6. Localized subsidence in (a–d) North Salt Lake and (e and f) Lehi. (a and d) Cumulative vertical deformation in North Salt Lake during 2004–2010 and 2015–2016, respectively. (b) Cumulative nonlinear vertical deformation against precipitation. (c) Vertical deformation velocity in North Salt Lake during 2015–2016, with the area of subsidence enlarged. (e) Cumulative vertical deformation in Lehi during 2015–2016. (f) Vertical deformation velocity in Lehi during 2015–2016, with a subsiding site enlarged, to show the development of fissures. The error bars in panels a, d, and e are the standard deviations of the deformation estimates within 200 m of the selected target.

production. For example, the net uplift of the hydrological unit highlighted by the high-resolution deformation map (Figure 2a) is marked by seasonality and large RMSE due to significantly fluctuating deformation, while the other hydrological units with no detectable motions are marked by no seasonality and small residuals. On the other hand, the industrial production is characterized by no seasonality and large RMSE due to accelerated or quasi-linear trend of deformation.

5.2. Long-Term Deformation Due to a Delayed Response to the Prolonged Head Changes

The aquifer skeletal response to changes in subsurface water levels is not instantaneous and may take years to appear as surface deformation. According to a U.S. Geological Survey report (Burden et al., 2005) on the groundwater conditions during 1975–2005 in Salt Lake Valley, water levels in the principal aquifer mostly declined, probably due to increased withdrawal and decreased precipitation. The greatest water level decline occurred south of Holladay and east of Midvale (dark gray shaded areas in Figure 7), which is on the southern and southeastern parts of the valley. However, detectable subsidence was observed only at the Salt Lake City segment of Wasatch Range on the eastern part of the valley, and the subsidence signal is minor (<5 mm/year). As comparison, the long-term inelastic subsidence in Central Valley, California, can be up to 60 cm/year (Farr & Liu, 2014). The water level measurements at the gauge no. 404356111503901 (40°43′57″N, 111°50′39″W; Figure S10a) close to the area of
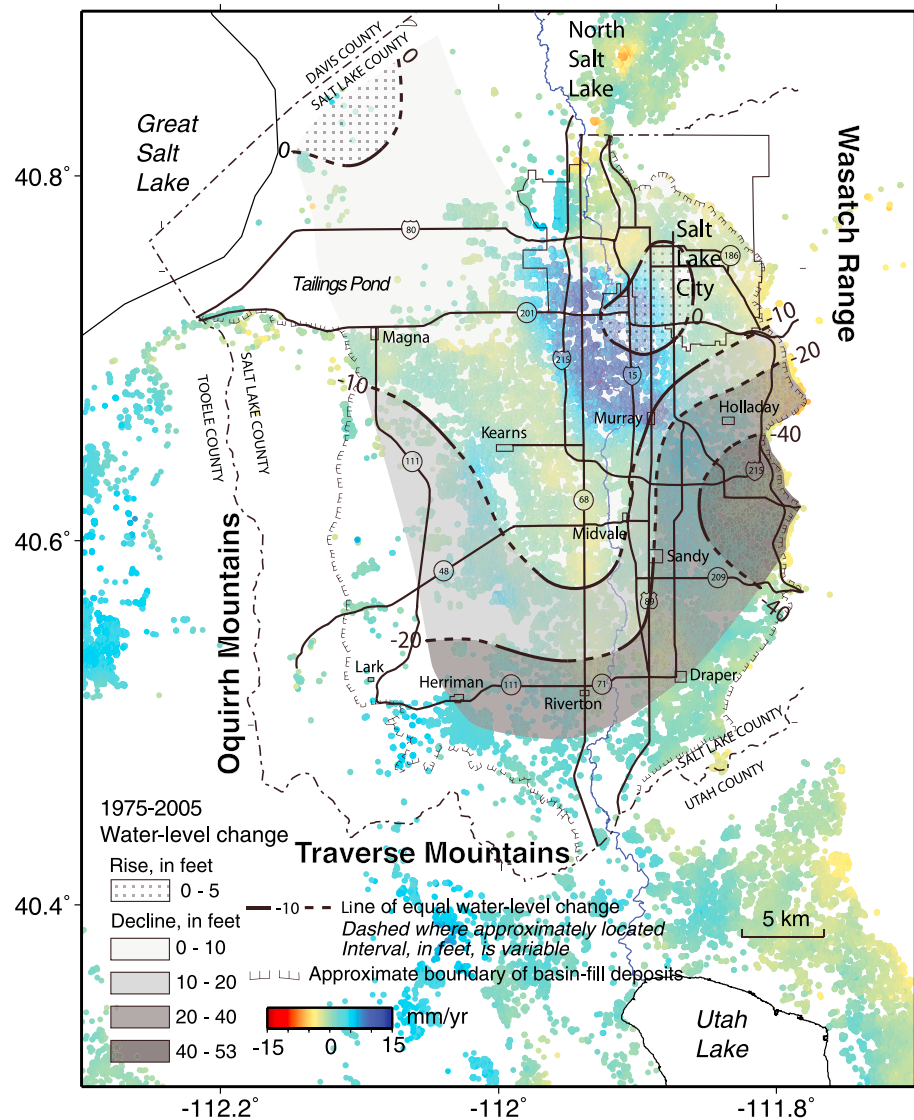
Figure 7. Map of groundwater level changes from 1975 to 2005, digitalized from Burden et al. (2005), superimposed on the long-term vertical deformation velocity derived from 2004 to 2010 ENVISAT data.

subsidence show that the lowest level on record is around 1935, and the water level recovered and dropped interchangeably with relative lows around 1962, 1980, 1992, and 2005. The water levels during 2004–2010 obviously exceeded the lowest level. Overall, the inelastic component in the subsidence should be nonexistent or negligible.

Remarkably, groundwater level has increased in the downtown area and the northwestern part of the valley (dotted areas in Figure 7), which is consistent with the ground uplift derived from the ENVISAT data. We infer that the uplift signature over the UAOI may result from the on-site water level increase. When the seasonal recharge of groundwater exceeds the amount of discharge over a long time span, the accompanying water level increase leads to net uplift of the surface when the vertical hydraulic conductivity is low enough to avoid rapid fluid diffusion (Miller et al., 2017). This is consistent with a large decay coefficient (−0.1 to −0.01) and thus slow equilibrium to the head changes at the heart of the UAOI. Interestingly, the water level change map of 1975–2005 shows that there is a small outstanding area with slight water level rise (0–5 feet or 1.5 m) in Salt Lake City. However, the map for 1970–2000 (Burden et al., 2000) shows a border area with increased water level at the foot of the Wasatch Range. This area extends southwest to form an elliptical shape with its long axis oriented at an azimuth of approximately 45° east of

north in the water level change map of 1980–2010 (Burden et al., 2010), which is characterized with small water level decline (0–10 feet or 3 m) in the most recent map of 1985–2015 (Burden et al., 2015). A similar resemblance between the spatial patterns of groundwater level and displacement in a particular time interval, rather than the earlier or more recent time, has also been observed in Gulf Coast aquifers (Qu et al., 2015).

We have shown that the net uplift at UAOI coincides with the area of net water level increase from 1975 to 2005, suggesting that the net uplift has a lagged response to the head increase, probably decades ago. However, the water level was not consistently increasing during 1975–2005. According to the monthly-to-yearly recorded water level data since 1931 at gauge no. 404506111523301 (40°45'07"N, 111°52'37"W; Figure S10b) near the eastern boundary of our UAOI, the water level only increased during 1963–1982 (by ~2 m) and 1990–1995 (by ~1 m), while the water level mainly fluctuated for the time intervals of 1931–1963 and 1995 onward. The timing and magnitude of the vertical strain for an aquifer also may depend on other parameters, including aquifer thickness, permeability, and storage states, which can change with lithology, or with seismic shaking (e.g., Chaussard et al., 2014).

The water-level-change map used in this study was based on an interpolation of measurements at about a dozen of gauges distributed in the aquifer basin, with a temporal sampling rate of only once per year (Burden et al., 2000, 2005, 2010, 2015). Therefore, the contours of water level change may not be perfectly constrained due to the sparsely distributed gauges. On the other hand, because the ground deformation is approximately proportional to hydraulic head changes, the surface deformation map with estimates covering most of the aquifer can improve the resolution of water level changes (e.g., Chen et al., 2016).

5.3. Salt Lake Valley, UT, and Santa Clara Valley, CA: Similarity and Distinction

There are similarities in the aquifers below Santa Clara Valley, CA, and Salt Lake Valley, UT. They are both located under densely populated areas, and both systems possess faults that function as hydrologic barriers, disrupting the subsurface flow of groundwater and modulating the long-term ground deformation (Schmidt & Bürgmann, 2003).

Santa Clara Valley had a subsidence history from 1916 to 1982 (Poland & Ireland, 1988), in contrast to later uplift from 1992 to 2011 due to water recharge (Schmidt & Bürgmann, 2003; Chaussard et al., 2014). We have also observed an uplift signal in Salt Lake Valley from 2004 to 2010, yet the reason behind the uplift could be different for the two aquifer systems. For Santa Clara Valley, the observed elastic strain is in response to anthropogenic withdrawal and later remedial actions of fluid injection. However, there is no evidence of consistent fluid injection before or during 2004–2010 in Salt Lake Valley, suggesting that the aquifer in Salt Lake Valley responds elastically to the natural hydrological process. Alarmed at the social and environmental problems caused by the uncontrolled groundwater withdrawal in Santa Clara Valley, particular attention needs to be paid to the prolonged water level decline in most areas of Salt Lake Valley (Figure 7; Burden et al., 2000, 2005, 2010, 2015). Once irreversible inelastic subsidence occurs, it may cause critical damage to the roads and other infrastructures. Additionally, the valley may face the threat of saltwater intrusion and permanently contaminating the water source if subsidence was to be so pronounced as to allow the groundwater level near the Great Salt Lake to drop below the water level of the lake itself.

6. Conclusions

We have measured the ground deformation over two time intervals (2004–2010 and 2015–2016) over Salt Lake Valley using multitemporal InSAR analysis. The InSAR-derived deformation maps highlight seasonal oscillating cycles of uplift and decline as well as a long-term net uplifting area southwest of downtown Salt Lake City. Spatially, the net uplifting area falls within the aquifer systems' discharge area and is bounded by existing faults. The maps of deformation velocity, the seasonality, and the decay coefficient help us better evaluate the existing boundaries of principal aquifers and identify some previously unknown fault segments, suggesting that the embedded faults disrupt the groundwater flow and partition the hydrological units. Temporally, the time series deformation measurements provide insights into the time scale over which the groundwater exchanged. The cross correlation with hydrological observations, such as precipitation and water discharge rate, reveals that the ground deformation is modulated by both water recharge and discharge processes. The large seasonal oscillations reflect the rapid redistribution of

groundwater. In one location, the long-term uplift corresponds to the prolonged increase in hydraulic head and thus the pore pressure. In addition, two localized subsiding sites were identified through the analysis in North Salt Lake and Lehi, which are likely the result of anthropogenic activities rather than natural hydrological processes.

References

Agram, P. S., Jolivet, R., Riel, B., Lin, Y. N., Simons, M., Hetland, E., et al. (2013). New radar interferometric time series analysis toolbox released. *Eos, Transactions American Geophysical Union*, *94*(7), 69–70. https://doi.org/10.1002/2013EO070001

Agram, P. S., & Simons, M. (2015). A noise model for InSAR time-series. *Journal of Geophysical Research: Solid Earth*, *120*, 2752–2771. https://doi.org/10.1002/2014JB011271

Amelung, F., Galloway, D. L., Bell, J. W., Zebker, H. A., & Laczniak, R. J. (1999). Sensing the ups and downs of Las Vegas: InSAR reveals structural control of land subsidence and aquifer-system deformation. *Geology*, *27*(6), 483–486. https://doi.org/10.1130/0091-7613

Arnow, T., Van Horn, R., & LaPray, R. (1970). The pre-Quaternary surface in the Jordan Valley, Utah, in Geological Survey Research 1970. U.S. Geol. Surv. Professional Paper 700-D, D257-D261.

Arnow, T., & Mattick, R. E. (1968). Thickness of valley fill in the Jordan Valley east of Great Salt Lake, Utah, in Geological Survey Research 1968. U.S. Geol. Surv. Professional Paper 600-B, B79-B82.

Bell, J. W., Amelung, F., Ramelli, A. R., & Blewitt, G. (2002). Land subsidence in Las Vegas, Nevada, 1935–2000: New geodetic data show evolution, revised spatial patterns and reduced rates. *Environmental and Engineering Geoscience*, *8*(3), 155–174. https://doi.org/10.2113/8.3.155

Berardino, P., Fornaro, G., Lanari, R., & Sansosti, E. (2002). A new algorithm for ground deformation monitoring based on small baseline differential SAR interferograms. *IEEE Transactions on Geoscience and Remote Sensing*, *40*(11), 2375–2383. https://doi.org/10.1109/TGRS.2002.803792

Black, B. D., Lund, W. R., Schwartz, D. P., Gill, H. E., & Mayes, B. H. (1996). Paleoseismology of Utah, volume 7—Paleoseismic investigation on the Salt Lake City segment of the Wasatch fault zone at the South Fork Dry Creek and Dry Gulch sites, Salt Lake County, Utah. Utah Geol. Surv. Special Study 92, 22 p.

Burden, C. B., Allen, D. V., Cederberg, J. R., Fisher, M. J., Freeman, M. L., Downhour, P., et al. (2010). Groundwater conditions in Utah, spring of 2010 (Cooperative Investigations Report No. 51). Salt Lake City, UT: Utah Department of Natural Resources, Division of Water Resources.

Burden, C. B., Allen, D. V., Danner, M. R., Walzem, V., Cillessen, J. L., Kenney, T. A., et al. (2005). Ground-water conditions in Utah, spring of 2005 (Cooperative Investigations Report No. 46). Salt Lake City, UT: Utah Department of Natural Resources, Division of Water Resources.

Burden, C. B., Sory, J. D., Danner, M. R., Johnson, K. K., Kenny, T. A., Brockner, S. J., et al. (2000). Ground-water conditions in Utah, spring of 2000 (Cooperative Investigations Report No. 41). Salt Lake City, UT: Utah Department of Natural Resources, Division of Water Resources.

Burden, C. B., et al. (2015). Groundwater conditions in Utah, spring of 2015 (Cooperative Investigations Report No. 56). Salt Lake City, UT: Utah Department of Natural Resources, Division of Water Resources.

Casagrande, A. (1932). The structure of clay and its importance in foundation engineering. In *contributions to Soil Mechanics 1925-1940* (pp. 72–113). Boston: Boston Society of Civil Engineering.

Casagrande, A. (1936). Determination of preconsolidation load and its practical significance. Proc. 1st Conf. Soil Mech. and Found. Eng. (Vol. 3). Am. Soc. Civil Engineering, 60–64.

Chaussard, E., Bürgmann, R., Shirzaei, M., Fielding, E. J., & Baker, B. (2014). Predictability of hydraulic head changes and characterization of aquifer system and fault properties from InSAR-derived ground deformation. *Journal of Geophysical Research: Solid Earth*, *119*, 6572–6590. https://doi.org/10.1002/2014JB011266

Chen, J., Knight, R., Zebker, H. A., & Schreüder, W. A. (2016). Confined aquifer head measurements and storage properties in the San Luis Valley, Colorado, from spaceborne InSAR observations. *Water Resources Research*, *52*, 3623–3636. https://doi.org/10.1002/2015WR018466

Domenico, P. A., & Mifflin, M. D. (1965). Water from low-permeability sediments and land subsidence. *Water Resources Research*, *1*(4), 563–576. https://doi.org/10.1029/WR001i004p00563

Farr, T. G., & Liu, Z. (2014). Monitoring subsidence associated with groundwater dynamics in the Central Valley of California using interferometric radar. In *Remote Sensing of the Terrestrial Water Cycle* (chap. 24, pp. 397–406). Hoboken, NJ: John Wiley. https://doi.org/10.1002/%209781118872086.ch24

Fattahi, H., Agram, P., & Simons, M. (2017). A network-based enhanced spectral diversity approach for TOPS time-series analysis. *IEEE Transactions on Geoscience and Remote Sensing*, *55*(2), 777–786. https://doi.org/10.1109/TGRS.2016.2614925

Ferretti, A., Prati, C., & Rocca, F. (2000). Nonlinear subsidence rate estimation using permanent scatterers in differential SAR interferometry. *IEEE Transactions on Geoscience and Remote Sensing*, *38*(5), 2202–2212. https://doi.org/10.1109/36.868878

Ferretti, A., Prati, C., & Rocca, F. (2001). Permanent scatterers in SAR interferometry. *IEEE Transactions on Geoscience and Remote Sensing*, *39*(1), 8–20. https://doi.org/10.1109/36.898661

Galloway, D., Jones, D. R., & Ingebritsen, S. E. (1999). Land subsidence in the United States. U.S. Geol. Surv. Circular 1182.

Hanson, R. T. (1989). Aquifer-system compaction, Tucson Basin and Avra Valley, Arizona. U.S. Geol. Surv. Water-Resources Investigations 88-4172.

Hooper, A. (2008). A multi-temporal InSAR method incorporating both persistent scatterer and small baseline approaches. *Geophysical Research Letters*, *35*, L16302. https://doi.org/10.1029/2008GL034654

Hooper, A. (2010). A statistical-cost approach to unwrapping the phase of InSAR time series. European Space Agency Special Publication, ESA SP-677.

Hu, X., Wang, T., Pierson, T. C., Lu, Z., Kim, J. W., & Cecere, T. H. (2016). Detecting seasonal landslide movement within the Cascade landslide complex (Washington) using time-series SAR imagery. *Remote Sensing of Environment*, *187*, 49–61. https://doi.org/10.1016/j.rse.2016.10.006

Jiang, H., Feng, G., Wang, T., & Bürgmann, R. (2017). Toward full exploitation of coherent and incoherent information in Sentinel-1 TOPS data for retrieving surface deformation: Application to the 2016 Kumamoto (Japan) earthquake. *Geophysical Research Letters*, *44*, 1758–1767. https://doi.org/10.1002/2016GL072253

Kim, J. W., Lu, Z., Jia, Y., & Shum, C. K. (2015). Ground subsidence in Tucson, Arizona, monitored by time-series analysis using multi-sensor InSAR datasets from 1993 to 2011. *ISPRS Journal of Photogrammetry and Remote Sensing*, *107*, 126–141. https://doi.org/10.1016/j.isprsjprs.2015.03.013

Lambert, P. M. (1995). Numerical simulation of ground-water flow in basin-fill material in Salt Lake Valley, Utah. *Utah Department of Natural Resources Technical Publication No. 110–B*, 58 p.

Lu, Z., & Danskin, W. (2001). InSAR analysis of natural recharge to define structure of a ground-water basin, San Bernardino, California. *Geophysical Research Letters*, *28*(13), 2661–2664. https://doi.org/10.1029/2000GL012753

Lu, Z., & Dzurisin, D. (2014). *InSAR imaging of Aleutian Volcanoes: Monitoring a volcanic arc from space* (390 pp.). Berlin: Springer-Verlag. https://doi.org/10.1007/978-3-642-00348-6

Massonnet, D., & Feigl, K. L. (1998). Radar interferometry and its application to changes in the Earth's surface. *Reviews of Geophysics*, *36*(4), 441–500. https://doi.org/10.1029/97RG03139

Mattrick, R. E. (1970). Thickness of unconsolidated to semiconsolidated sediments in Jordan Valley, Utah. U.S. Geol. Surv. Prof. Paper 700-C, C119-C124.

Miller, M. M., & Shirzaei, M. (2015). Spatiotemporal characterization of land subsidence and uplift in Phoenix using InSAR time series and wavelet transforms. *Journal of Geophysical Research: Solid Earth*, *120*, 5822–5842. https://doi.org/10.1002/2015JB012017

Miller, M. M., Shirzaei, M., & Argus, D. (2017). Aquifer mechanical properties and decelerated compaction in Tucson, Arizona. *Journal of Geophysical Research: Solid Earth*, *122*, 8402–8416. https://doi.org/10.1002/2017JB014531

Nelson, G. L. (1982). Vertical movement of ground water under the Merrill Field Landfill, Anchorage, Alaska. U.S. Geol. Surv. Open-File Report 82 (1016).

Neuman, S. P., & Witherspoon, P. A. (1972). Field determination of the hydraulic properties of leaky multiple aquifer systems. *Water Resources Research*, *8*(5), 1284–1298. https://doi.org/10.1029/WR008i005p01284

Poland, J. F., & Ireland, R. L. (1988). Land subsidence due to withdrawal of fluids. *Reviews in Engineering Geology*, *2*, 187–269.

Qu, F., Lu, Z., Zhang, Q., Bawden, G. W., Kim, J. W., Zhao, C., & Qu, W. (2015). Mapping ground deformation over Houston–Galveston, Texas using multi-temporal InSAR. *Remote Sensing of Environment*, *169*, 290–306.

Reeves, J. A., Knight, R., Zebker, H. A., Kitanidis, P. K., & Schreüder, W. A. (2014). Estimating temporal changes in hydraulic head using InSAR data in the San Luis Valley, Colorado. *Water Resources Research*, *50*, 4459–4473. https://doi.org/10.1002/2013WR014938

Reinisch, E. C., Cardiff, M., & Feigl, K. L. (2016). Graph theory for analyzing pair-wise data: Application to geophysical model parameters estimated from interferometric synthetic aperture radar data at Okmok volcano, Alaska. *Journal of Geodesy*, *91*(1), 9–24. https://doi.org/10.1007/s00190-016-0934-5

Riel, B., Simons, M., Agram, P., & Zhan, Z. (2014). Detecting transient signals in geodetic time series using sparse estimation techniques. *Journal of Geophysical Research: Solid Earth*, *119*, 5140–5160. https://doi.org/10.1002/2014JB011077

Riley, F. S. (1969). Analysis of borehole extensometer data from central California. *International Association of Scientific Hydrology. Publication*, *89*, 423–431.

Saar, M. O., & Manga, M. (2003). Seismicity induced by seasonal groundwater recharge at Mt. Hood, Oregon. *Earth and Planetary Science Letters*, *214*(3-4), 605–618. https://doi.org/10.1016/S0012-821X(03)00418-7

Schmidt, D. A., & Bürgmann, R. (2003). Time-dependent land uplift and subsidence in the Santa Clara valley, California, from a large interferometric synthetic aperture radar data set. *Journal of Geophysical Research*, *108*(B9), 2416. https://doi.org/10.1029/2002JB002267

Shirzaei, M., Bürgmann, R., & Fielding, E. J. (2017). Applicability of Sentinel-1 terrain observation by progressive scans multitemporal interferometry for monitoring slow ground motions in the San Francisco Bay Area. *Geophysical Research Letters*, *44*, 2733–2742. https://doi.org/10.1002/2017GL072663

Sneed, M. (2001). Hydraulic and mechanical properties affecting ground-water flow and aquifer system compaction, San Joaquin Valley, California. U.S. Geol. Surv. Open File Report 1(35).

Sneed, M., Borchers, J. W., Kayen, R. E., Carkin, B. A., Ellett, K. M., Wheeler, G. A., & Brocher, T. M. (2007). Hydromechanical response characterization by integration of geophysical and hydrological data, San Lorenzo, California. AGU Fall Meeting, Abstracts, J23A-1007.

Snyder, N. P, & Lowe, M. (1998). Map of recharge areas for the principal valley-fill aquifer, Ogden Valley, Weber County, Utah. Utah Geological Survey Map 176, 16 p., scale 1:75,000.

Starn, J. J., Bagtzoglou, A. C., & Green, C. T. (2015). The effects of numerical-model complexity and observation type on estimated porosity values. *Hydrogeology Journal*, *23*(6), 1121–1128. https://doi.org/10.1007/s10040-015-1289-3

Thiros, S. A. (2003). Hydrogeology of shallow basin-fill deposits in areas of Salt Lake Valley, Salt Lake County, Utah. U.S. Geol. Surv. Water-Resources Investigations Report 03-4029.

Thiros, S. A., Bexfield, L. M., Anning, D. W., & Huntington, J. M. (2010). Section 2.-conceptual understanding and groundwater quality of selected basin-fill aquifers in the southwestern United States. U.S. Geol. Professional Paper 1781.

Wallace, J., & Lowe, M. (2009). Ground-water quality classification for the principal basin-fill aquifer, Salt Lake Valley, Salt Lake County, Utah. Utah Geol. Surv., Open File Report 560.